WILEY | Hindawi

Research Article

Investigation into the Pore Structure and Multifractal Characteristics of Shale Reservoirs through N_2 Adsorption: An Application in the Triassic Yanchang Formation, Ordos Basin, China

Zhikai Liang [iD],[1,2] **Zhenxue Jiang** [iD],[1,2] **Zhuo Li** [iD],[1,2] **Fenglin Gao,**[3] **and Xiaoqing Liu**[4]

[1]*State Key Laboratory of Petroleum Resources and Prospecting, China University of Petroleum, Beijing 102249, China*
[2]*The Institute of Unconventional Oil & Gas Science and Technology, China University of Petroleum, Beijing 102249, China*
[3]*Development and Research Center, China Geological Survey, Beijing 100037, China*
[4]*College of Optoelectronic Engineering, Chongqing University, Chongqing 400044, China*

Correspondence should be addressed to Zhenxue Jiang; jiangzhenxuecup@126.com and Zhuo Li; lizhuopaper@163.com

To understand the pore structure and heterogeneity of pore size distribution (PSD) is essential for revealing fluid mechanics and evaluating the utilization of unconventional resources. In this study, there are multiple shale examples collected from the Chang 7 section in the Ordos Basin for the investigation was conducted on the basis of various experiments on total organic carbon (TOC), X-ray diffraction (XRD), and nitrogen gas adsorption, through scanning electron microscopy (SEM) and multifractal method. The multifractal characteristic parameters, including the width of singularity spectra ($\Delta\alpha$), Hurst exponent (H), D_1/D_0, and nitrogen gas adsorption, were used to find out about the characteristics of pore development and to quantify the complexity and heterogeneity of pore structure. Depending on the exact mineral composition, the Yanchang Formation of Chang 7 shales is classified into either silty mudstone (SM) or muddy siltstone lithofacies (MS). According to the investigative results, the Chang 7 lacustrine shale features a complex pore system with the pores ranging from 1.5 to 10 nm in diameter. Besides, mesopores contribute significantly to the total pore volume (TPV) and total surface area (TSA). As for TPV and TSA of the SM lithofacies in the samples under investigation, they are nearly 1.09–1.78 and 0.80–1.72 times greater as compared to the MS lithofacies samples. The dominant types of reservoir spaces include organic matter (OM) pore and interparticle pore which are related to inorganic minerals. The value of $\Delta\alpha$ is higher for MS lithofacies than for SM lithofacies, indicating a greater heterogeneity of PSD in the MS lithofacies. The pore structure of MS lithofacies is determined mainly by TOC and siliceous mineral content, whereas the influencing factors for SM lithofacies are TOC and clay mineral content. There is a significant relationship between multifractal parameters and pore structure parameters for both SM and MS lithofacies. The TOC of SM and MS lithofacies exhibits a close correlation with $\Delta\alpha$, suggesting that the pores in organic matter are dominated by those nanopores with a complex and heterogeneous pore structure. The rock composition of the lithofacies can affect $\Delta\alpha$ to a varying extent, which means that the minerals have an evident impact on the heterogeneity of MS and SM lithofacies.

1. Introduction

Unconventional oil and gas are considered the most important future energy sources worldwide [1–3]. In various kinds of unconventional energy sources, the shale displays the self-sourced and reservoir feature, which shows the foreseeable enormous economic value and exploration and development prospect [1, 4]. Contrary to the conventional reservoir, the shale pore structure is characterized with a quite wide range by nanoscale to macroscale and shows a more complicated and heterogeneous pore network, as well as low porosity and permeability [5]. It is well understood that it closely links the pore structures to the oil and gas transport mechanism and storage capabilities in the shale [6]. The pore

structure can support important parameters, including the pore volume (PV), pore surfer area (SA), average pore diameter (APD), and pore size distribution (PSD), which have been executed by many researchers [1, 4, 7]. Previous investigations have shown that the nanopore feature is of great significance in the shale formation evaluation. Thus, understanding the pore structure of shale help effectively the estimation of the resource potential and production performances.

Various methods have been widely applied to describe the shale pore size distribution indirectly including small-angle neutron scattering (SANS), high mercury intrusion porosimetry (HMIP), gas adsorption, and nuclear magnetic resonance (NMR) and display the pore geometry characterization including field-emission scanning electron microscope (FE-SEM), atomic force microscopy (AFM), and nano-CT [2, 3, 7–21]. Among these, gas adsorption has been proven an effective method to characterize the pore structure quantitatively. However, these methods could not quantify the heterogeneous and complex geometry of nanoscale pore structures. Fractal theory, a tool for description statistical self-similarity, is an effective method to analyze the irregularity and heterogeneity of PSD in the soil system, coals, shales, and other porous materials [22–26]. In the previous studies, the extensive method has been used to measure fractal dimensions including Frenkel–Halsey–Hill (FHH) model, thermodynamics model, NMR model, image processing, V-S model, and HMIP model [13, 27–33].

It is highlighted that the conventional fractal model is not adequate quantitatively to evaluate the irregularity and local scale properties of the pore system [24–26, 34]. As a fractal theory extension, the multifractal theory can discompose into intertwined fractal subsets and describe the spatial distribution of measures quantitatively [35]. Through the generalized fractal dimensions and singularity strength spectra, the multifractal spectral function provides more detailed information about the integral and local heterogeneity of PSD [26, 36]. Compared with previous studies on single fractal theory, several studies were conducted on the multifractal characteristics of shale reservoirs by using LF-N_2 methods [24, 25, 34].

In this study, 12 examples from the Chang 7 shale in Ordos Basin, from the different wells, were collected and conducted the different lithofacies with TOC, XRD, nitrogen gas adsorption, SEM, and multifractal method. The goal of this study can be explained as to (1) explicitly classify the main lithofacies types by mineral composition, (2) illustrate the pore structure development from the different lithofacies, (3) compare the heterogeneity of the pore structures from the different lithofacies via the multifractal theory, and (4) reveal the main influence factors of the pore structures and the multifractal parameters.

2. Geological Setting

The Ordos Basin is a large remnant cratonic sedimentary basin covering approximately 25×10^4 km^2 area, located in the northern-central part of China with a whole stratigraphic and weak deformation [16, 32, 37]. The basin con-

sists of six units including the Yimeng uplift, the Weibei uplift, the Western margin thrust belt, the Tianhuan depression, the Jinxi flexural fold belt, and the Yishan Ramp [38]. In this study area, the Yishan slope, is a remarkable monocline with a gentle 1-3° dip angle from east to west, and it is composed of rare faults and slight structure deformation (Figures 1(a) and 1(b)) [15, 39]. As a multicycle evolutionary stage basin, the basement of Ordos Basin consists of crystalline rocks which are from Archean Eocene and Paleoproterozoic [40]. In the Latest Middle Triassic period, the fluvial and terrestrial siliciclastic sediments were deposited under the intact depositional cycle with the thickness of about 3000~4000 m [32, 41]. As the most main source unit, the 7th member of the Triassic Yanchang formation was formed in the semideep water of the lake sedimentary environment with 10-40 m, which was considered the most favorable formation for the shale-gas generation (Figure 1(d)) [16, 42–43]. The lithology of Chang 7 lacustrine shale formation is mainly composed of thick gray-black, dark-gray, petroliferous shales, and thin layer argillaceous siltstones [16, 32, 37]. It has been reported that the TOC of Chang 7 ranges from 1.6%-14% and mainly type I and II; the hydrogen index is generally 50-638 mg HC/g TOC; the hydrocarbon potential ($S_1 + S_2$) is 5.5-142.41 mg/g [32, 44].

3. Samples and Methods

3.1. Samples and Experiments. In the study area, a series of samples from shale formations were selected from the seven drillings of exploration wells (Figure 1(c)). All examples were analyzed pore structure and heterogeneity from the depth of 1150.31 to 1663.39 m.

Before the tests, the shale examples were powdered less than a 40-60 mesh size and placed into the D8 Advance X-ray diffractometer at 40 kV and 40 mA to study the mineralogical content. The Rock-Eval pyrolysis was used to evaluate the TOC content of the examples quantified. All the examining examples were placed into a drying oven for at least 8 h at 110°C to avoid the influence of residual gas and bound water. The SEM image can observe the nanomicropore morphology and structure directly. To avoid the interference factor, the pretreatment of samples was cut into slices and polished with argon ion to produce an undamaged and reproducible surface. The instrument was Quanta 450 field emission scanning electron microscope (FE-SEM) to obtain typical higher resolution images and acquire detailed information of the pore morphology [43]. As a wide method, the N_2 gas adsorption was used to analyze the pore structure and provide more information about PSD in the size of 0.3 to 300 nm. The N_2 adsorption analysis was conducted in a Micromeritics ASAP-2020 apparatus under a temperature of 196°C conditions. In the process of nitrogen adsorption experiment, the amount of liquid nitrogen was recorded in the relative equilibrium adsorption pressure scope of 0.01–0.99 (P/P_0). Several parameters including surface area (SA) and pore volume (PV) were calculated by the BET and BJH theoretical with the range of 2-200 nm [45].
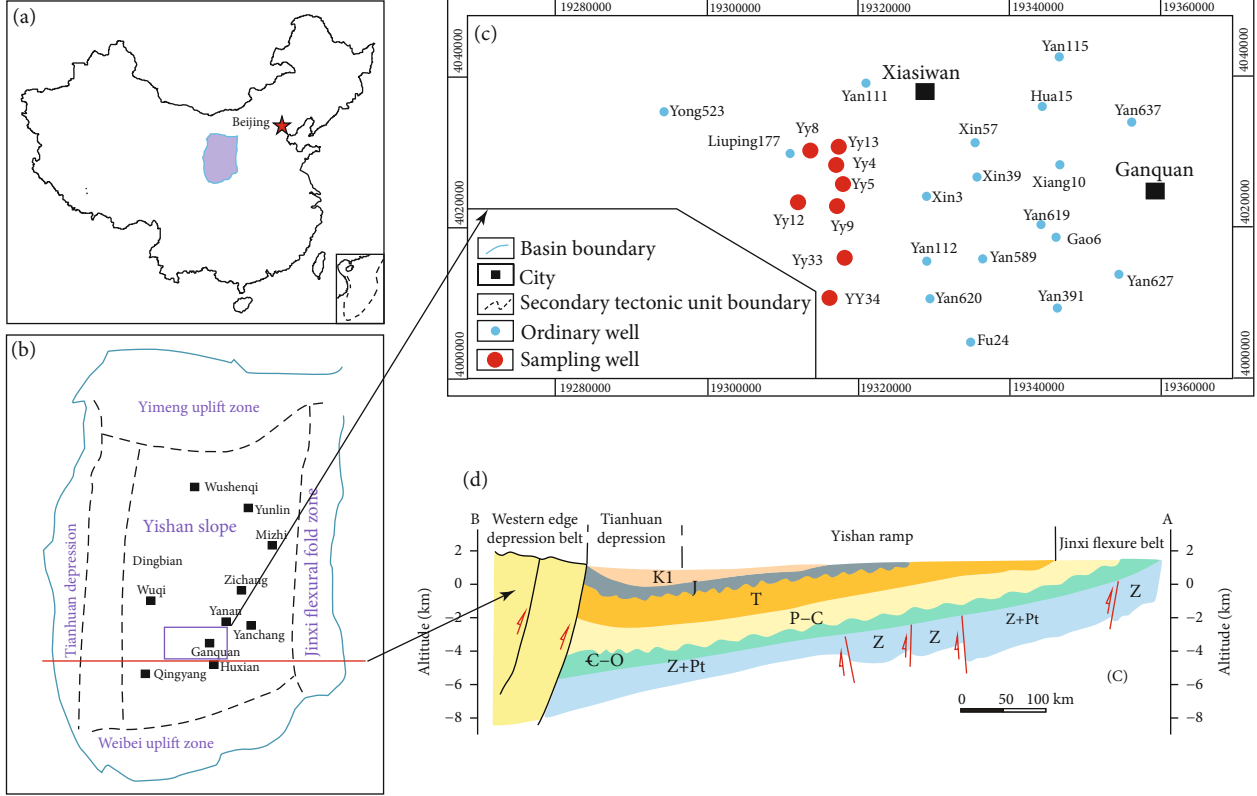
FIGURE 1: The location of the Ordos Basin in China (a and b) and the study area location of sampling wells (modified from Shan et al. [32]); stratigraphic column of the study area.

3.2. Multifractal Theory. As the extension of single fractal dimension theory, multifractal formalism was used to describe the complex structures and the heterogeneity of rock pore structures. In the previous studies, detailed information on multifractal processes was provided [2, 5, 19, 23–25, 33, 35, 36, 46, 47].

In this procedure, the Box-counting method is a widely used and popular tool to confirm a set of different boxes with a similar equal length of ε to cover the target object L, where $\varepsilon = L/2^k$ $(k = 0,1,2,3,\cdots)$. In this study, the relative pressure (P/P_0) was taken as the length ε. $N(\varepsilon)$ is defined as the total number of boxes with the size of ε to cover the PSD curve from the gas adsorption measurements [24, 25]. For heterogeneous porous media, the probability mass distribution $P_i(\varepsilon)$ for the ith box with a scale ε could be represented as [26, 48]

$$ P_i(\varepsilon) = \frac{N_i(\varepsilon)}{\sum_{i=1}^{N(\varepsilon)} N_i(\varepsilon)}, \tag{1} $$

where $P_i(\varepsilon)$ is the probability density distribution, $N_i(\varepsilon)$ is the space of adsorbed nitrogen of partition ith box with the size of ε, and $N(\varepsilon)$ is the total volume of gas.

If the samples show the multifractal property, the probability density distribution will have the relationship with the size ε and will be obtained from [49]

$$ P_i(\varepsilon) \propto \varepsilon^{\alpha_i}, \tag{2} $$

where α_i is the singularity strength (Lipschitz-Hölder singularity exponent) and represents the density in the ith box.

Here, we defined the multifractally distributed properties of size ε with same the value expressed as

$$ N_\alpha(\varepsilon) \sim \varepsilon^{-f(\alpha)}, \tag{3} $$

where $f(\alpha)$ is the set of the fractal dimensions which indicates the fractal dimension of the boxes with the same or close a value of α.

The probability density distribution of the q for the size ε can be further weighted defined as [48]

$$ X(q,\varepsilon) = \sum_{i=1}^{N_i} P_i^q(\varepsilon) \sim \varepsilon^{\tau(q)}, \tag{4} $$

where $X(q,\varepsilon)$ is the partition function of q with scale ε and $\tau(q)$ is the mass scaling function, which can be expressed as [5, 26, 28, 50]

$$ \tau(q) = -\lim_{\varepsilon \longrightarrow 0} \frac{\log \sum_{i=1}^{N(\varepsilon)} P_i^q(\varepsilon)}{\log \varepsilon}. \tag{5} $$

The generalized multifractal dimension D_q can be defined as [51]

TABLE 1: Mineral composition, TOC, and lithofacies for Yanchang lacustrine shale samples in the study area.

Sample ID	Well	TOC (%)	Mineral composition (%)								Lithofacies
			Clay	Qz	Kfs	Pl	Cal	Dol	Py	Sd	
YY5-1	YY5	5.52	48	35	7	8			2		MS
YY7-1	YY7	3.72	43	37	5	13			2		MS
YY12-1	YY12	5.00	48	30	8	12			2		MS
YY13-1	YY13	4.10	42	37	9	9				3	MS
YY13-2	YY13	4.47	48	36	8	8					MS
YY13-4	YY13	6.01	43	42	2	8		3	2		MS
YY4-2	YY4	6.26	47	35		11	4		3		SM
YY9-1	YY9	5.42	48	28	5	7	10		2		SM
YY9-2	YY9	5.29	52	30	4	4	3	3		4	SM
YY5-2	YY5	3.82	51	26	3	4		16			SM
YY13-3	YY13	2.68	64	23	5	6			2		SM
YY5-3	YY5	2.33	55	32		10				3	SM

Qz: quartz; Kfs: K-feldspar; Pl: plagioclase; Cal: calcite; Dol: dolomite; Py: pyrite; Sd: siderite.

$$D_q = \frac{1}{q-1} \lim_{\varepsilon \longrightarrow 0} \frac{\log \sum_{i=1}^{N(\varepsilon)} P_i^q(\varepsilon)}{\log \varepsilon}. \tag{6}$$

By combining Equations (5) and (6), the relationship between multifractal spectrum $f(\alpha)$ and singularity strength $\alpha(q)$ can be determined from $\tau(q)$ and q with using the Legendre transformation [26, 28], respectively:

$$f(\alpha) = q\alpha(q) - \tau(q), \tag{7}$$

$$\alpha(q) = \frac{d\tau(q)}{dq}. \tag{8}$$

The material and method section should contain sufficient detail so that all procedures can be repeated. It may be divided into headed subsections if several methods are described.

4. Result

4.1. Characteristics of the Shale Samples. Mineralogically, the XRD results of Chang 7 lacustrine shale core examples are listed in Table 1, which shows the dominant minerals are quartz and clay minerals, followed by some carbonate and other minerals. Quartz is generally 23%-42%, with an average value of 32.6%, for Chang 7 lacustrine shale which is close to the transitional shale and country to the marine shale. The total clay minerals occupy 23%-42%, with an average value of 32.6%, of the whole shale, followed by plagioclase and dolomite, with contents ranging from 4% to 13% and 3%–16%, and the average values are 8.3% and 7.3%, respectively. In addition, part of the examples has some minerals such as pyrite, siderite, and calcite, with low content of about 10% (Table 2). In the clay minerals, I/S is the dominant content ranging from 36% to 86% with an average of 51.9%, which recommends the lacustrine shale of Chang 7 is in the a period of middiagenesis. The content of illite mineral contents is close to the smectite, with the

TABLE 2: Clay mineral composition for Yanchang lacustrine shale samples.

Sample ID	Depth (m)	TOC (%)	Clay composition (%)				
			K	Chlorite	Illite	I/S	Smectite
YY5-1	1450.2	5.52		17	29	54	15
YY7-1	1150.3	3.72	17	14	24	45	20
YY12-1	1618.2	5.00		17	32	51	15
YY13-1	1194.4	4.10		19	29	52	15
YY13-2	1201.5	4.47		29	28	43	15
YY13-4	1360.1	6.01		23	39	38	15
YY4-2	1532.9	6.26	4	5	22	69	20
YY9-1	1663.4	5.42		23	24	53	15
YY9-2	1671.3	5.29		14	33	53	15
YY5-2	1455.0	3.82		17	26	57	15
YY13-3	1203.5	2.68		19	25	56	15
YY5-3	1457.9	2.33		10	21	69	15

former ranging between 21% and 39% (average of 27.7%) and the latter from 15 to 20% (average of 15.8%).

Lithofacies characterization is the fundamental indicator to demonstrate the sedimentary facies analysis and sedimentary environments of shales [8, 52]. With the success of shale exploration and development and sweet spot evaluation, lithofacies studies are identified as a significant step in the process of shale evaluation. The previous study has suggested the sedimentary environments of Chang 7 are the delta and deep lacustrine with multiple pore structure and complex pore geometry feature [32]. Thus, a full description of the lacustrine shale reservoir is necessary to be associated with their lithofacies. Many classification systems originate from (1) logging, core explanation, and diagenesis [53]; (2) deep neural network [54]; and (3) lithological characteristics and rock sections. According to the marine, transitional, and lacustrine shale lithofacies classification, in this study, combined with the previous lithofacies division scheme, the

result of XRD is associated with the value of OM to form the lithofacies classification in the study area [55, 56]. However, due to the stability of region tectonics of Ordos Basin, the effect of thermal evolution in examples is not significant [57]. The thermal evolution degree of Ro in Chang 7 is too slightly volatile to neglect. The classification scheme introduces the content of TOC and mineral component data, which reflects the shale petrological and petrophysical characteristics, with effective and universal relevance principle in the Ordos Basin.

The classification standard usually categorizes different lithofacies in shales based on TOC, lithology, or mineral composition. In order to classify the shale lithofacies, TOC and mineral composition have been analyzed. Based on the content of three main components, including siliceous components (quartz+feldspar), carbonate components (calcite, dolomite), and muddy components (clay), these main lithofacies can be classified. Using this main classification, several subgroups are identified within a major category. Figure 2 shows the shale lithofacies classification with TOC and mineral compositions in the study area. According to the normalization experimental collected data, the mineral component and TOC value can be divided into two main lithofacies, which are silty mudstone (SM) and muddy siltstone (MS).

4.2. Analysis of N_2 Adsorption/Desorption Isotherms. The N_2 adsorption isotherms including the sharpness of adsorption and desorption branch curves can be used to analyze the pore morphology and the surface. A total of 12 examples were analyzed and showed the similar "S" type in the low-pressure N_2 adsorption-desorption branches. In the branch of adsorption, the adsorption quantity increases rapidly from a slow rate increasing the relative pressure (Figure 3). The increase rate is attributed to the adsorption phase monolayer and multilayer transformation. With the relative pressure close to 0.8, the adsorption curves rise very more rapidly, which fits Henry's law. According to the geometrical morphology characteristics of hysteresis, the hysteresis loop displays various shapes, which are generated by the capillary condensation effect and illustrate the existence of mesopores in the Chang 7 samples [58]. From the data in Figure 3, it is apparent that a sharp desorption step point at relative pressure P/P_o 0.4–0.5, named K point or cavitation mechanism in the desorption branch of some samples, indicating that the wide cavities are connected with narrower necks. Compared with fluid pressure in the neck, the metastable fluid in the cavity has low vapor-liquid equilibrium pressure, and the neck effectively "blocks" desorption from the cavity [59, 60].

According to the IUPAC, the different lithofacies samples show a various hysteresis loop. In the MS lithofacies, the hysteresis loops of YY13-1 belong to the complex H2 and H3, which corresponded to "ink-bottle shaped" pores. The H3 type is represented by the YY12-1 samples, reflecting that shale nanoscale pores are mainly opened pores [32]. The hysteresis loops of the YY13-4, YY13-2, YY5-1, and YY16-9 samples belong to the H4 type, indicating that shale nanoscale pores with larger pore size contain opened

pores and may have some semiclosed pores. The hysteresis loop of SM lithofacies is characterized by both H1 and H3 curves of the IUPAC [61]. The hysteresis loops of YY4-2, YY5-2, YY5-3, and YY9-1 belong to the H1 indicating the development of the semiclosed pore. The H3 type is represented by the YY9-2 and YY13-2, indicating that the opening pores. It is worth noticing that the hysteresis loop result is consistent with the SEM images.

4.3. Pore Structure from N_2 Adsorption. Table 3 is a summary of the pore structure parameters including the BJH pore volume and BET surfer area, extracted from N_2 adsorption isotherms. The SM lithofacies shales have the higher pore volume and pore surfer area, ranging from $0.038 \, cm^3/g$ to $0.056 \, cm^3/g$ and $9.922 \, m^2/g$ to $14.000 \, m^2/g$, with an average of $0.044 \, cm^3/g$ and $12.162 \, m^2/g$, respectively. Regarding MS lithofacies, the accumulated pore volumes range from $6.96 \, cm^3/g$ to $11.4 \, cm^3/g$, with an average of $8.54 \, cm^3/g$. The SA in the MS lithofacies shale samples lies between $1.89 \, m^2/g$ and $2.27 \, m^2/g$, with an average of $2.13 \, m^2/g$. In general, the pore volume and surface area of the SM lithofacies in the studied samples are almost 1.09-1.78 and 0.80-1.72 times greater than the pore volume and surface area of the MS lithofacies samples. Figure 4 shows that pores with pore diameters less than 10 nm are developed in both types of lithofacies. The SM lithofacies general features have higher pore volume values than the MS lithofacies.

4.4. Scanning Electron Microscopy. According to the results of the SEM, the OM pore, InterP pore, IntarP pore, and microfracture were identified in the Chang 7 Formation shales in Figure 5 [9, 32]. The OM pores can be observed clearly with various shapes including elliptic, strip, nested, and irregularity or bubble-like generally ranging from several nanometers to hundreds of nanometers (Figure 5) [9, 12]. The OM pore morphological characteristics between the rigid particles including the quartz and feldspar are affected by the compaction effect in Figures 5(b), 5(d), and 5(g). It is worth noting that there is a complex structure inside the spongy OM pore and interlinked with each other, which can form favorable connection of the OM-pore network (Figure 5(b)). The microfractures are presented with shrinkage cracks in the OM, and the wall of the fractures has two morphological characteristics including smooth and straight (Figure 5(c)), or rough and zigzagged (Figure 5(f)), which all have a significant effect on hydrocarbon production [9, 12]. In addition, the OM pores in the Yanchang shale are developed and show strong heterogeneity. Figures 5(e) and 5(g) show the enlarged square areas from Figures 5(d) and 5(h), respectively. The sponge-like pores were also observed clearly in the adjacent margin of OM with pores 30–400 nm in size. The OM pore remaining space can be found in the rigid grains and the microcrystal quartz are developed in the OM particles (Figure 5(i)).

Some pyrite intercrystallite pores with multiple types of geometry in Figure 6(a) [9]. Some of the pyrite aggregates are filled with OM and inorganic minerals and developed the OM pore inside (Figure 6(b)). Intragranular pores associated with clay form strip shapes or sheet shapes, and the
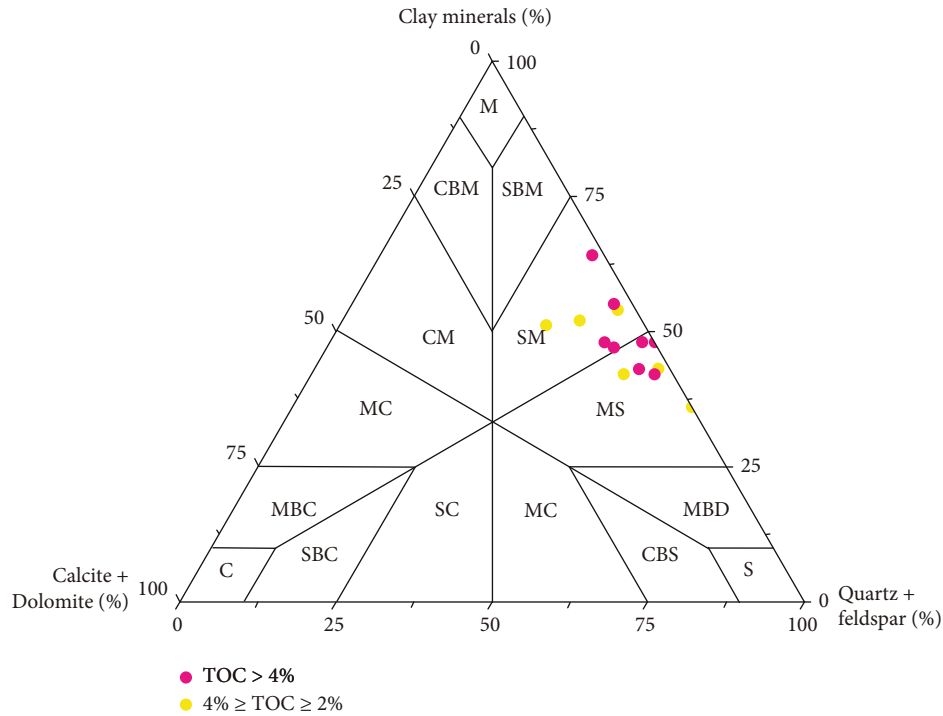
FIGURE 2: Ternary diagram of lithofacies classification with mineralogy shale samples investigated from the Chang 7 formation shales in the Erdos area [55]. M: mudstone; S: siltstone; C: carbonatite; SA: siliceous mudstone; CM: calcareous mudstone; MS: muddy siltstone; CS: calcareous siltstone; MC: muddy carbonatite; SC: siliceous carbonatite; SBM: siliceous-bearing mudstone; CBM: calcareous-bearing mudstone; MBS: mud-bearing siltstone; CBS: calcareous-bearing siltstone; MBC: mud-bearing carbonatite; SBC: siliceous-bearing carbonatite.
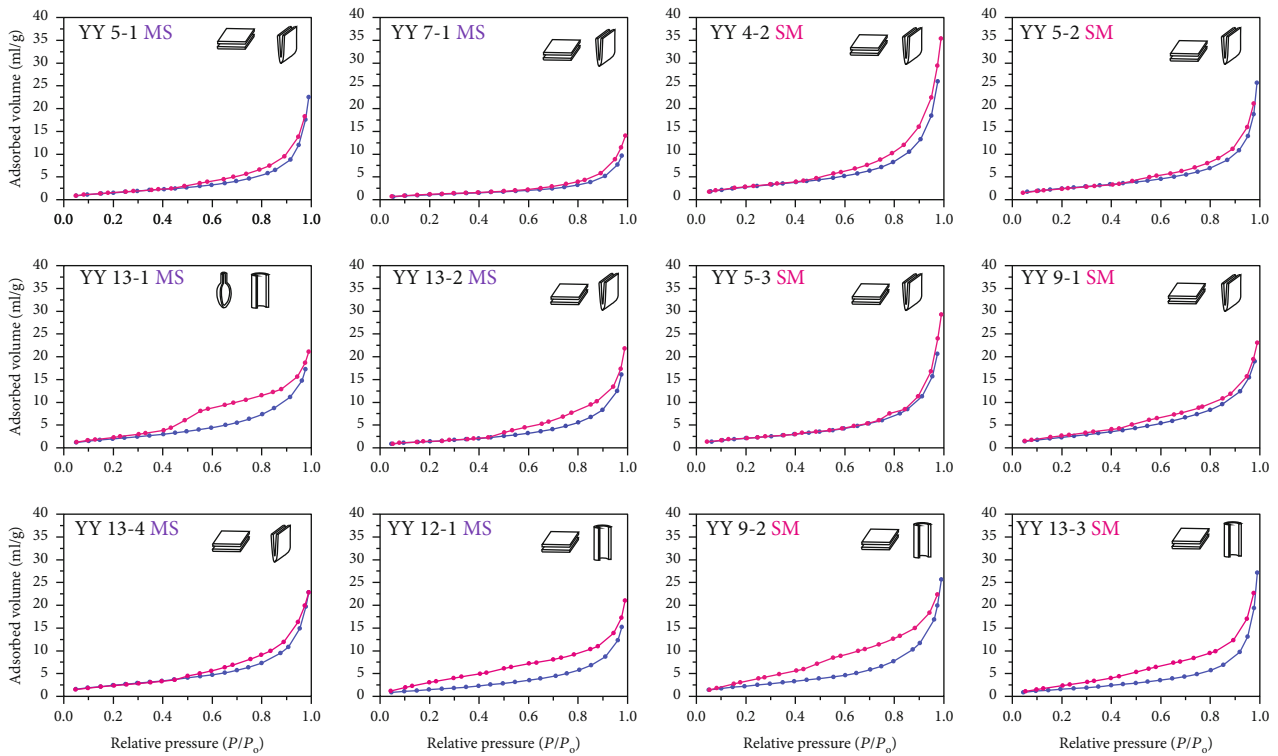

FIGURE 3: Low-pressure N_2 isotherms for the Chang 7 shale samples.

TABLE 3: Pore structure parameters of MS and SM lithofacies from low-pressure N_2 adsorption data.

| Samples ID	TOC (%)	Pore volume			Pore surfer area			Lithofacies
		Micropore	Mesopore	Macropore	Micropore	Mesopore	Macropore	
YY4-2	6.26	0.001	0.027	0.028	2.565	10.121	1.314	SM
YY5-2	3.82	0.001	0.020	0.019	2.149	8.503	0.872	SM
YY5-3	2.33	0.001	0.023	0.023	1.751	8.753	1.008	SM
YY9-1	5.42	0.000	0.025	0.013	0.795	12.112	0.522	SM
YY9-2	5.29	0.001	0.026	0.015	1.587	10.389	0.607	SM
YY13-3	2.68	0.000	0.020	0.023	1.180	7.675	1.067	SM
YY5-1	5.52	0.001	0.018	0.018	1.611	7.067	0.857	MS
YY7-1	3.72	0.001	0.013	0.009	1.695	4.573	0.428	MS
YY12-1	5.00	0.000	0.019	0.014	0.579	8.123	0.545	MS
YY13-1	4.10	0.000	0.023	0.011	1.164	10.037	0.434	MS
YY13-20	4.47	0.000	0.019	0.016	0.673	7.259	0.671	MS
YY13-4	6.01	0.001	0.023	0.013	2.084	9.602	0.619	MS

(a)

(b)
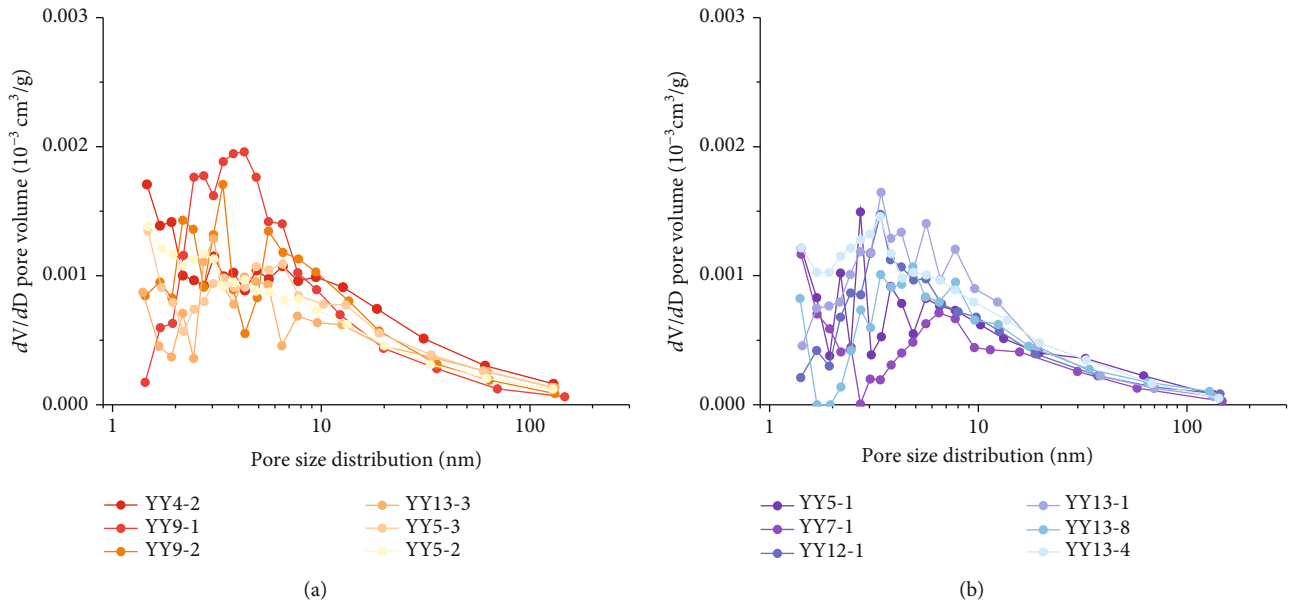
FIGURE 4: Pore size distribution of the Chang 7 samples obtained from nitrogen adsorption. (a) SM lithofacies. (b) MS lithofacies.

pores can be observed within laminar clay cleavages (Figure 6(c)). The clay cleavages display the annular shape with syntropy or random orientation (Figure 6(d)). Figure 6(e) shows that intergranular pores of rigid frameworks can be searched in among the edge rigid mineral grains, which are formed by the mechanical differences. Due to the effects of the organic acids, isolated dissolution pores also occur in feldspar grains, with a similar lower pore size and elliptical or circular shape (Figure 6(f)) [61]. Some pyrite grains are distributed in the laminar clay cleavages, forming the intergranular pores with parallel large diameters and the shape of elliptical, which increase the pore space (Figure 6(g)). Some pores are often found between clay sheets, and the foliated structure in the clay is affected by the rigid mineral during the compaction process of deposition (Figures 6(f) and 6(g)). Intergranular pores are rela-

tively large and mainly developed between clay minerals, quartz, or other brittle minerals.

4.5. Multifractal Characteristics of N_2 Adsorption. In this part, we analyze the multifractal characteristic behavior of the PSD by nitrogen adsorption. In practice, the multifractal spectra distribution ($\alpha \sim f(\alpha)$) and the generalized dimension ($q \sim D(q)$) are obtained in Figures 7 and 8, respectively. Dq spectra demonstrate a strong association with q, and the curve of Dq to q displays a decreasing monotone with q increasing from −10 to 10 at successive intervals. In the left branch (high probability measurement range), Dq decreases sharply as q increases. However, there is a slight decrease with increasing q in the right branch (low probability measurement range). The curve indicates the both the MS and SM lithofacies examples of PSD have multifractal behavior.
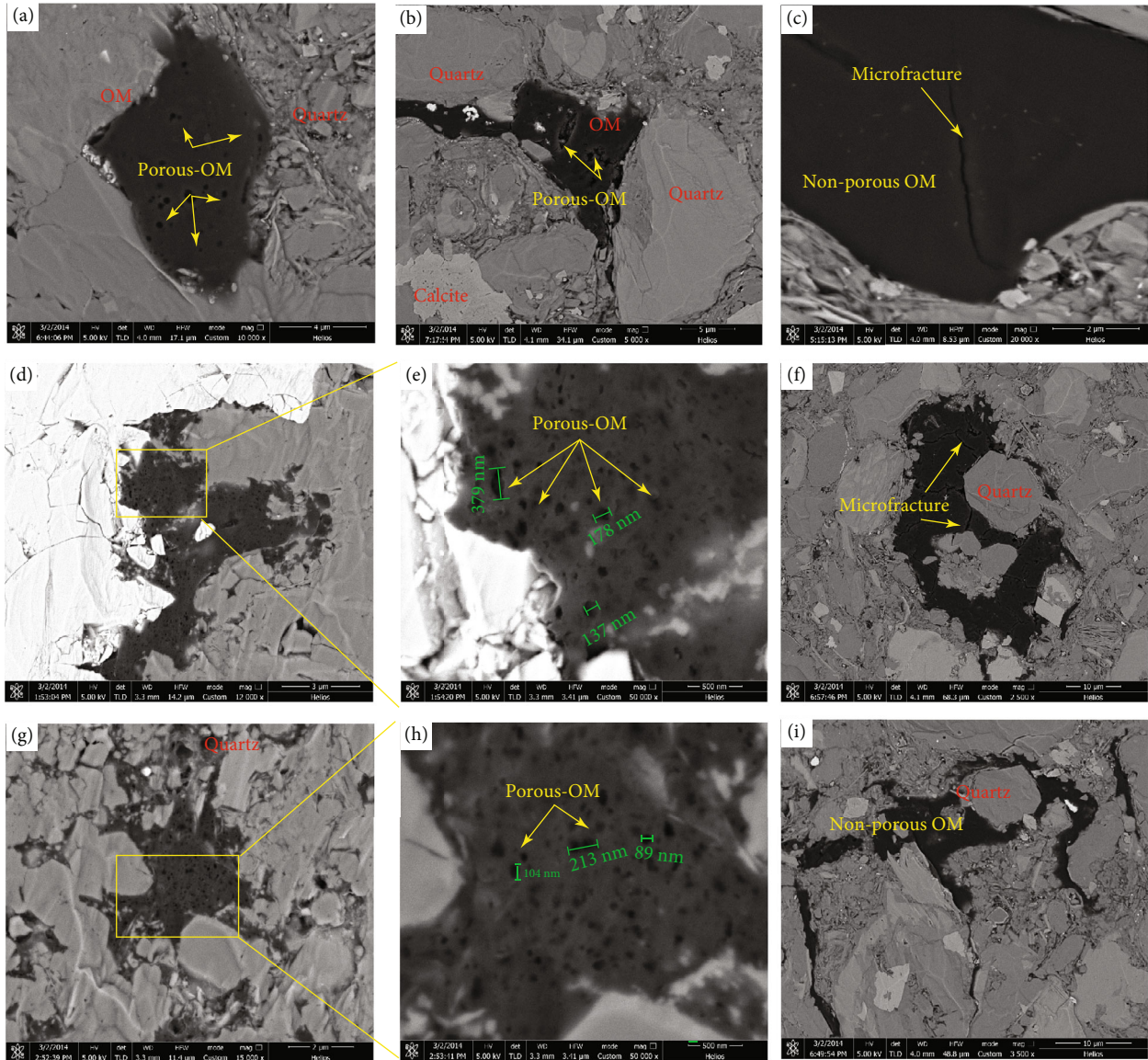
FIGURE 5: The SEM images of OM pores from MS and SM lithofacies Chang 7 lacustrine sample. (a, b) Porous OM-filled residual space of rigid grains (sample ID: YY5-3, 1437.9 m; YY7-1, 1150.3 m). (c) Microfractures separating organic matter with smooth edge (sample ID: YY9-1, 1663.4 m). (d) Porous OM with gas bubble shape pores among the particles (sample ID: YY13-4, 1360.1 m). (e) The expanded horizon of the image of (d). (f) Zigzagged with microcracks in the OM particles (sample ID: YY5-1, 1450.2 m). (g) Porous OM with irregular figures among particles (sample ID: YY4-2, 1532.2 m). (h) The expanded horizon of the image of (g). (i) Nonporous OM particle squeezed into mineral pores (sample ID: YY12-1, 1618.12 m).

Compared with the MS lithofacies, the Dq shows a wide variation range when $q < 0$ in the SM lithofacies. However, in $q > 0$, the MS lithofacies display a wide variation tendency. In the previous study, the D_0 is regarded as the capacity dimension; meanwhile, the D_0 and D_1 are the information dimension and correlation dimension [18, 24, 62–65]. The D_1/D_0 represents the concentration degree of the PSD along with the pore size intervals [65, 66]. The relationship between D_0, D_1, and D_2 show the order of $D_0 > D_1 > D_2$, revealing the significant multifractal characteristics in all studied Chang 7 examples. In addition, it is worth noticing that the Hurst exponent ($H = (D_2 + 1)/2$) is a parameter, which is the degree of the positive autocor-

relation and used to represent the degree of the pore connectivity [24, 64].

In Figure 8, the relationship between $f(a)$ and $\alpha(q)$ shows the shape of typical parabolic function curves, which is coincident with the previous research. To the left of the crest, the $f(a)$ increases as $\alpha(q)$ increases, while in the right of the crest, the $f(a)$ decreases as $\alpha(q)$ increases. The singularity strength length ($\Delta\alpha$) is an important parameter, which means the maximum probability (α_{max}) and minimum probability (α_{min}) interpolation from the PSD and characterizes the degree heterogeneity of the studied examples [24, 26, 28, 46].

In Figure 9, the mass exponent spectra $\tau(q)$ increase as the q increases. In the left branches, the $\tau(q)$ increases with
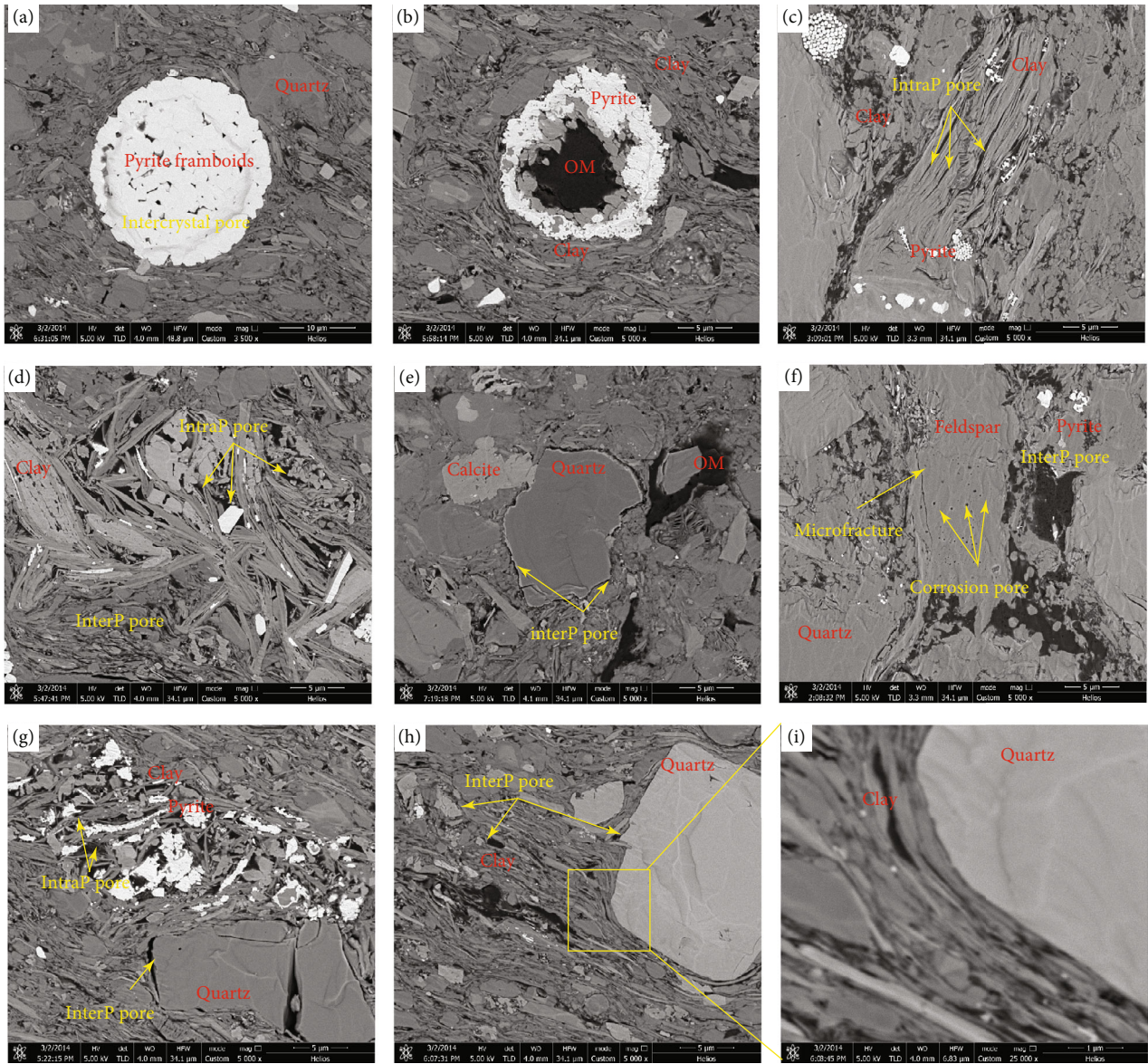
FIGURE 6: The SEM images of inorganic matter pores from MS and SM lithofacies Chang 7 lacustrine sample. (a) Single pyrite framboid which consists of euhedral crystals (sample ID: YY4-2, 1532.19 m). (b) The InterP pores of toroidal pyrite are commonly observed in the shale samples filled with OMs (sample ID: YY5-3, 1437.9 m). (c) Clay mineral intergranular pores showing narrow strip morphology (sample ID: YY5-2, 1455 m). (d) Porous OM among the clay flakes with isolated pyrite particles (sample ID: YY12-1, 1618.2 m). (e) Quartz intergranular pore (sample ID: YY9-1, 1663.4 m) (f) Intragranular dissolution pores formed by the dissolution of feldspar particles with dispersed distribution (sample ID: YY9-2, 1671.3 m). (g) Intragranular pores formed by randomly oriented clay mineral flakes (sample ID: YY13-3, 1203.5 m). (h) Clay minerals are influenced by brittle particle extrusion stress, and the clay flake is deformed (sample ID: YY13-4, 1360.1 m). (i) The expanded horizon of the image of (h).

a rapid rate, corresponding to $q < 0$. In the right branches, the $\tau(q)$ The curve is agreeing well with the previous research, which shows that different lithofacies samples have the multifractal characteristics.

4.6. Multifractal Parameters. The multifractal parameters are calculated and are presented in Table 4. The MS lithofacies values of $\Delta\alpha$ are in a range of 3.942–6.209 (with an average of 5.209), whereas significant differences are found in SM lithofacies of $\Delta\alpha$, which ranges from 3.919 to 6.023 (with an average of 4.645). The MS lithofacies values of $\Delta\alpha$ are

higher than that of SM lithofacies, indicating that the micropores of MS lithofacies samples are more heterogeneous. The MS lithofacies H values derived from N_2 adsorption multifractal vary from 1.377 to 1.583 with an average of 1.504, which is higher than that from the SM lithofacies. This indicated that MS lithofacies have favorable pore connectivity among different pores in the interval of 2–200 nm, compared with the SM lithofacies. When D_1/D_0 is closer to 1, it indicates that the particle distribution is mainly concentrated in the dense area, and when D_1/D_0 is closer to 0, it indicates that the particle distribution is concentrated in
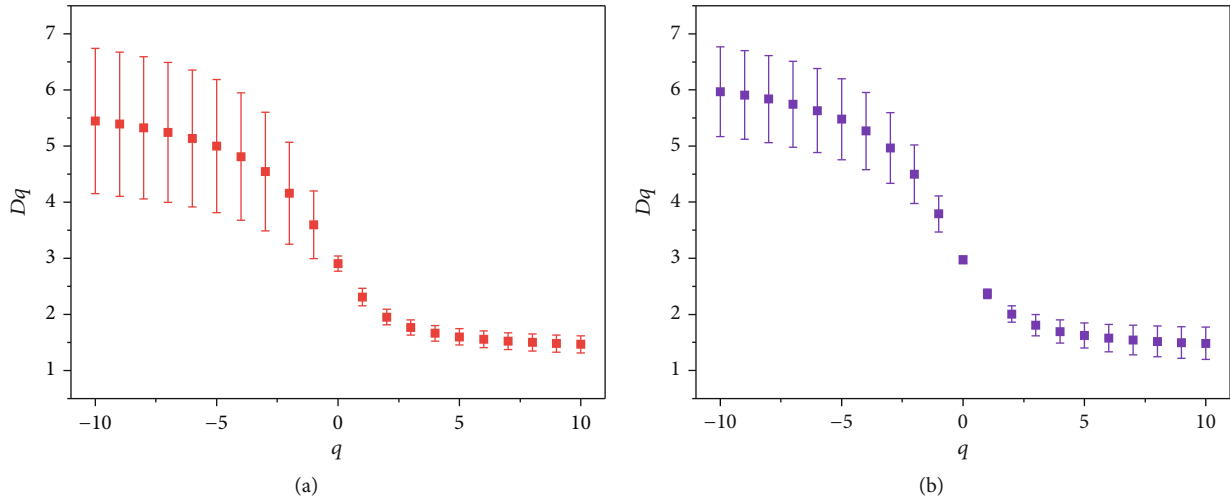
(a)

(b)

FIGURE 7: The generalized dimension (Dq) versus variable q computed from nitrogen adsorption. (a) SM lithofacies. (b) MS lithofacies. The error bars represent the standard deviation of measurements in twelve separate sample runs.
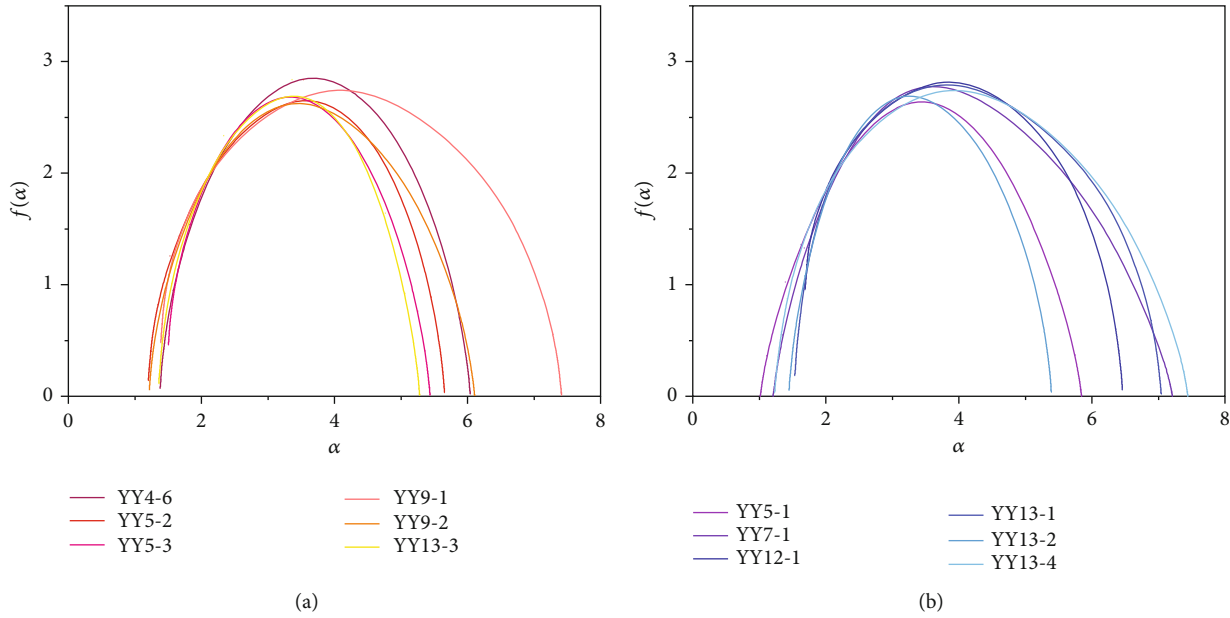

(a)

(b)

FIGURE 8: Multifractal spectra of Chang 7 shale pore structures obtained from nitrogen adsorption. (a) SM lithofacies. (b) MS lithofacies.

the sparse area [65]. The MS lithofacies D_1/D_0 values vary from 0.745 to 0.862 with an average of 0.797, indicating that MS lithofacies have a higher degree of concentration across a specific range of pore sizes obtained from N_2 adsorption.

5. Discussion

5.1. Effects of Composition on Pore Structure. In the section, the shale lithofacies (SM and MS) have similar trends in the relationship of pore structure parameters and composition (Figure 10). The PV in both MS and SM lithofacies shales show no obvious correlation with TOC content, whereas the SA display an obvious correlation with TOC (Figures 10(a) and 10(b)), which is consistent with the results of Shahezi shale and Nenjiang formation in Songliao

Basin [7, 24]. The SEM observation result is favorably verified showing the honeycomb and bubble shape OM pore (Figure 5). These relationships indicate shale of OM increasing would also have more interconnected honeycomb-like OM pore with a small pore diameter to provide more surfer area [67, 68]. The effects of clay mineral content on the TPV values are illustrated in Figure 10(c). There is no obvious good fitting line relationship in lithofacies, suggesting that the clay content is insufficient to provide low pore volume. The relationships of clay and surface area of MS and SM lithofacies shale samples are illustrated in Figure 10(d). The surface area has an obvious relationship with clay content, which results from the clay of MS and SM lithofacies which are mostly mixed illites and smectites (surfer area: 200 m²/g) providing external surfer area compared with
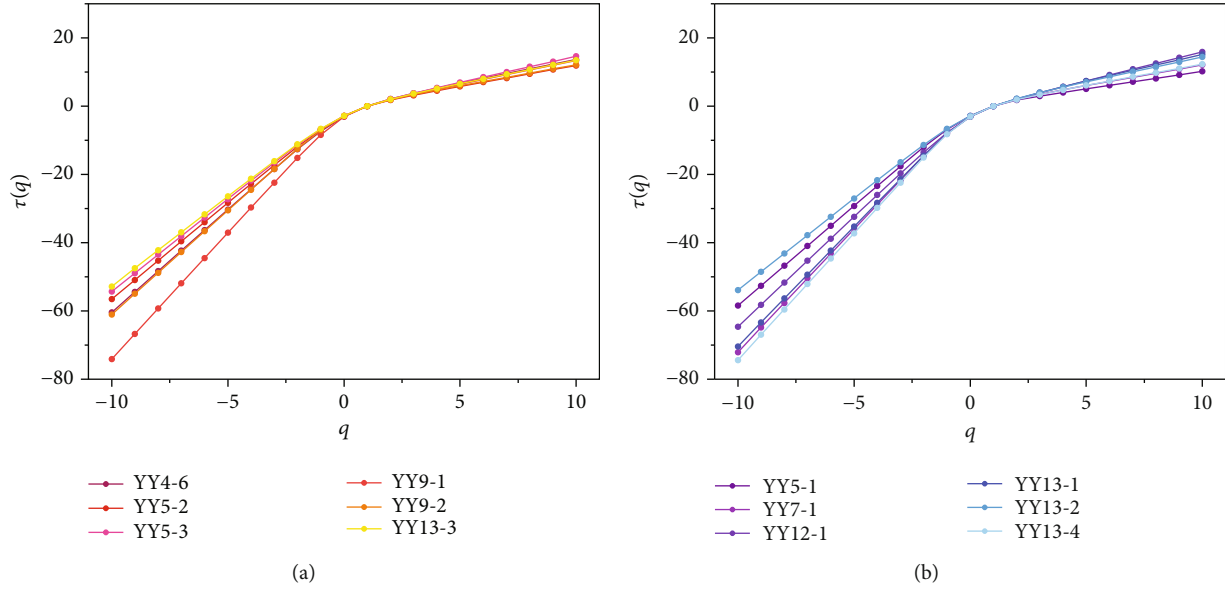
(a)

(b)

FIGURE 9: The relationship between the $\tau(q)$ and q of Chang 7 shale from nitrogen adsorption. (a) SM lithofacies. (b) MS lithofacies.

TABLE 4: Multifractal parameters of the SM and SM lithofacies calculated from low-pressure N_2 adsorption data.

Sample ID	Lithofacies	D_0	D_1	D_2	D_1/D_0	$D_{min} - D_{max}$	Δf	$\Delta \alpha$	Hurst	Rd
YY5-1		2.838	2.234	1.753	0.787	4.185	-2.838	4.829	1.377	0.020
YY7-1		3.041	2.453	2.023	0.807	5.208	-3.041	5.998	1.511	-0.922
YY12-1	MS	3.041	2.382	2.077	0.783	4.105	-2.086	4.769	1.539	-0.406
YY13-1		3.041	2.428	2.150	0.798	4.717	-2.853	5.505	1.575	-0.730
YY13-2		2.838	2.445	2.165	0.862	3.301	-2.784	3.942	1.583	-0.255
YY13-4		3.041	2.266	1.877	0.745	5.399	-3.007	6.209	1.439	-0.631
YY4-2		3.041	2.467	2.092	0.811	3.968	-2.970	4.660	1.546	-0.055
YY5-2		2.838	2.189	1.792	0.771	3.820	-2.696	4.448	1.396	0.208
YY5-3	SM	2.838	2.382	2.075	0.839	3.321	-2.378	3.930	1.538	-0.254
YY9-1		3.041	2.222	1.871	0.731	5.249	-2.561	6.023	1.436	-0.519
YY9-2		2.838	2.267	1.889	0.799	4.205	-2.784	4.889	1.445	-0.326
YY13-3		2.838	2.338	1.999	0.824	3.302	-2.722	3.919	1.500	0.089

other mineral compositions [69]. The TPV of MS and SM lithofacies have no apparent linear relationship with brittle mineral content (Figure 10(e)). In the SM lithofacies, the pores, in the clay and OM, are mainly concentrated and preserved around rigid grains, which indicates that the larger the quartz content is, the larger the value of TPV will be (Figure 10(e)). However, the number of pores is scarcely associated with the quartz content in the MS lithofacies, which agrees with the SEM observation results and the investigation on the $Es_1{}^3$ formation [68]. As shown in Figure 10(f), the negative relationships between quartz content and total surface area in the MS and SM lithofacies shales suggested that quartz is not the major contributor to the surface area of studied examples.

5.2. Evaluation of Pore Structure Performances on Multifractal Characteristics. The width of singularity spectra $\Delta \alpha$, Hurst exponent (H), and the concentration degree index

(D_1/D_0) are also commonly multifractal parameters. A correlation between pore structure parameters and the multifractal parameters of MS and SM lithofacies is apparent in Figure 11. $\Delta \alpha$ also shows a good negative correlation with the TPV in the Chang 7 shales between 2 nm and 200 nm, while $\Delta \alpha$ shows a positive relationship with total surfer area, which conclusion is consistent with recent studies concerning marine gas shale [13, 63]. With the pore volume increasing, the degree of pore heterogeneous decreases which can lead to the high $\Delta \alpha$ value, which is consistent with conclusions documented by other researchers [30, 32] (Figure 11(a)). Chang 7 shale with a larger surface area always has larger $\Delta \alpha$ indicating that the total surfer area has an obvious influence on the width of singularity spectra (Figure 11(d)). In order to understand the effect of total surfer area and pore volume characteristics on the pore connection, Hurst exponent and pore structure parameters are further plotted in Figures 11(b) and 11(e). The correlations
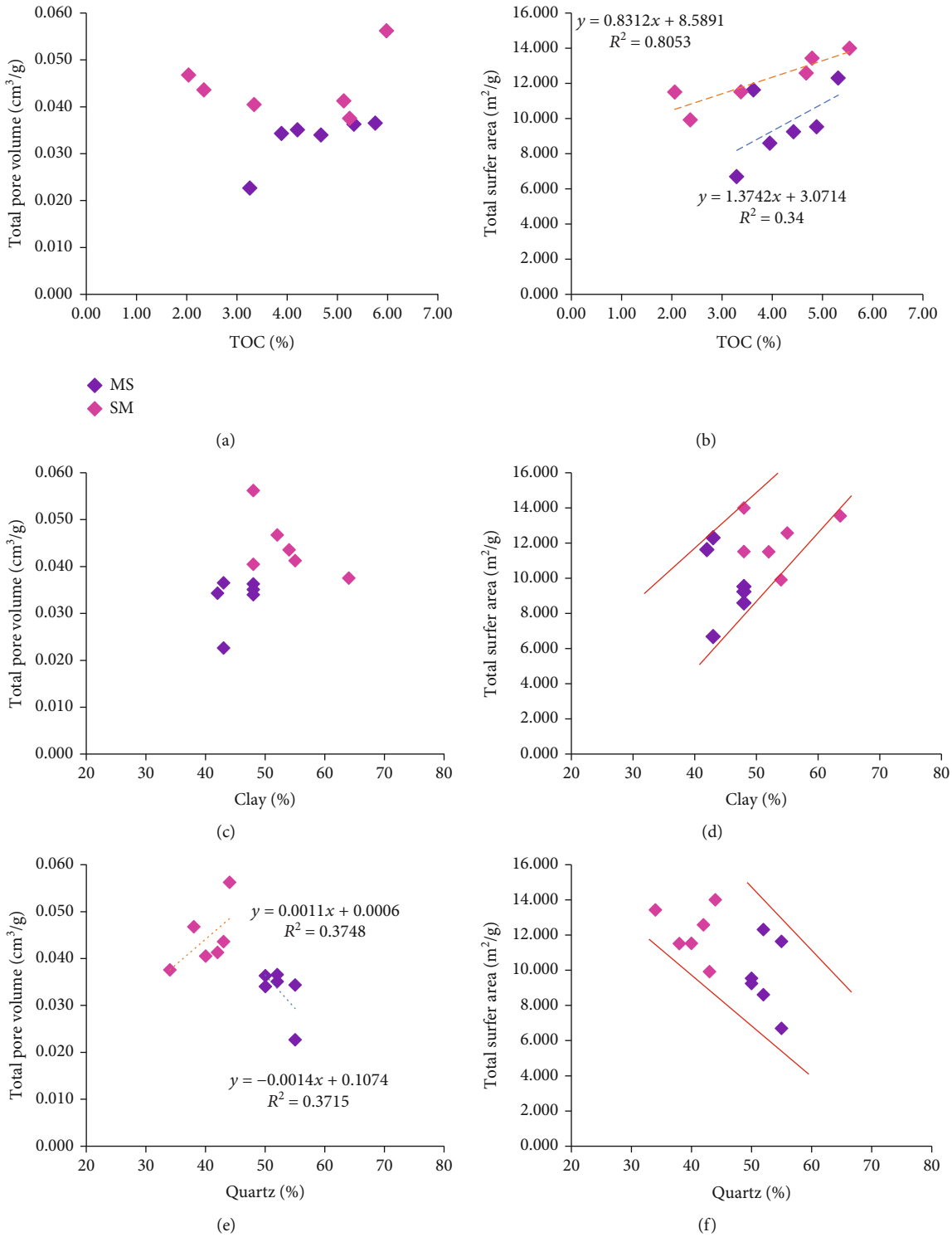
$$y = 0.8312x + 8.5891$$
$$R^2 = 0.8053$$

$$y = 1.3742x + 3.0714$$
$$R^2 = 0.34$$

(a)   (b)

(c)   (d)

$$y = 0.0011x + 0.0006$$
$$R^2 = 0.3748$$

$$y = -0.0014x + 0.1074$$
$$R^2 = 0.3715$$

(e)   (f)

FIGURE 10: Relationships between total pore volume and TOC (a), total surfer area and TOC (b), total pore volume and clay (c), total surfer area and clay (d), total pore volume and quartz (e), and total surfer area and quartz (f).

between the TPV and the Hurst exponent are no obvious, which indicates that the Hurst exponent is not an effective parameter that can describe the degree of pore connection in the interval of 2–200 nm (Figures 11(b) and 11(e)). Meanwhile, this no obvious relationship indicated that the Hurst exponent hardly impacted the total pore surfer and pore volume (Figures 11(b) and 11(e)). For the concentration degree index from N_2 adsorption, a positive relationship is found between D_1/D_0 and TPV (Figure 11(c)), while D_1/D_0 shows negative with the surfer area increasing (Figure 11(f)). Due
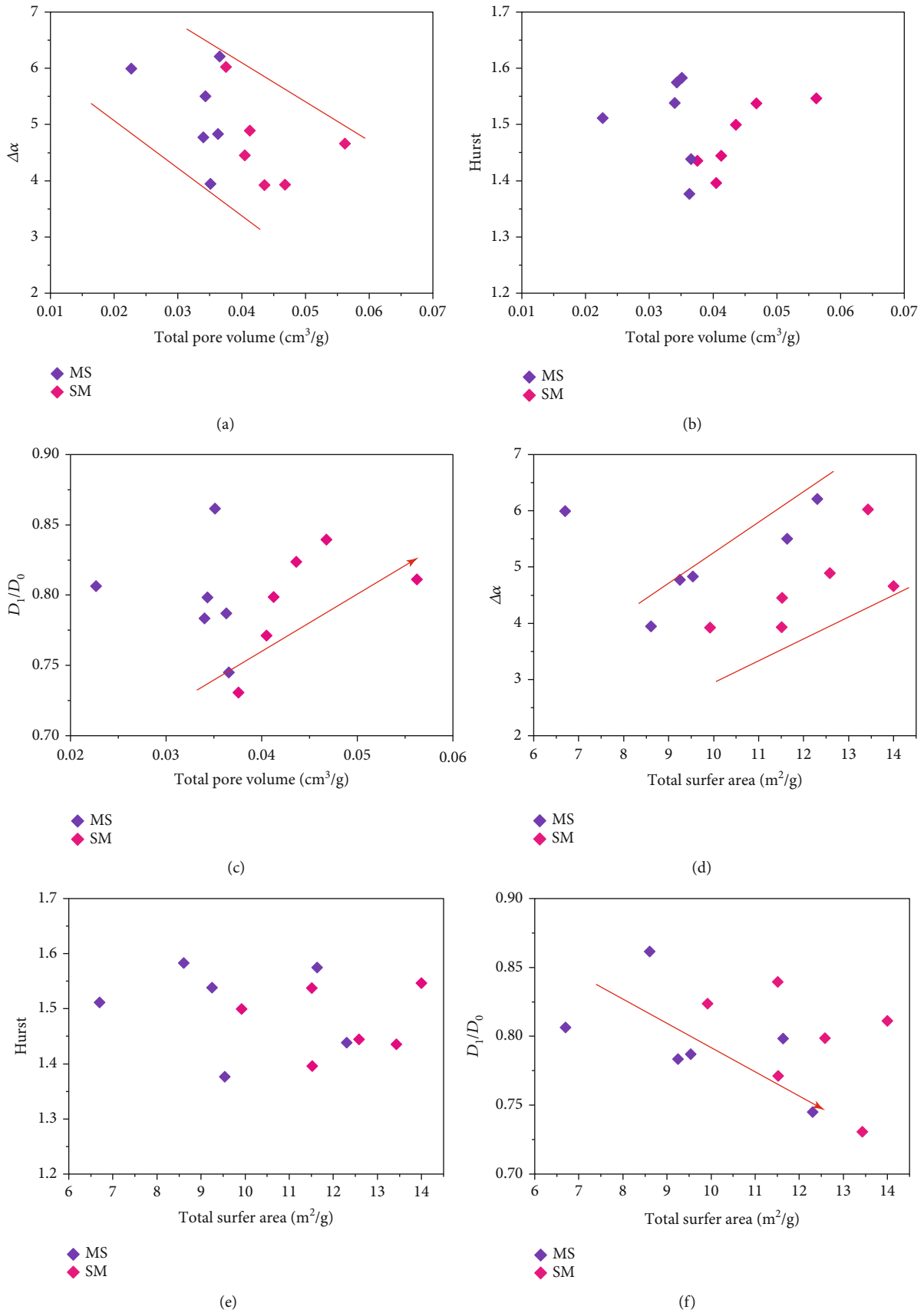
FIGURE 11: Relationships between total pore volume and $\Delta\alpha$ (a), total pore volume and Hurst (b), D_1/D_0 and total pore volume (c), total surface area and $\Delta\alpha$ (d), total surfer area and Hurst (e), and total surfer area and D_1/D_0 (f).
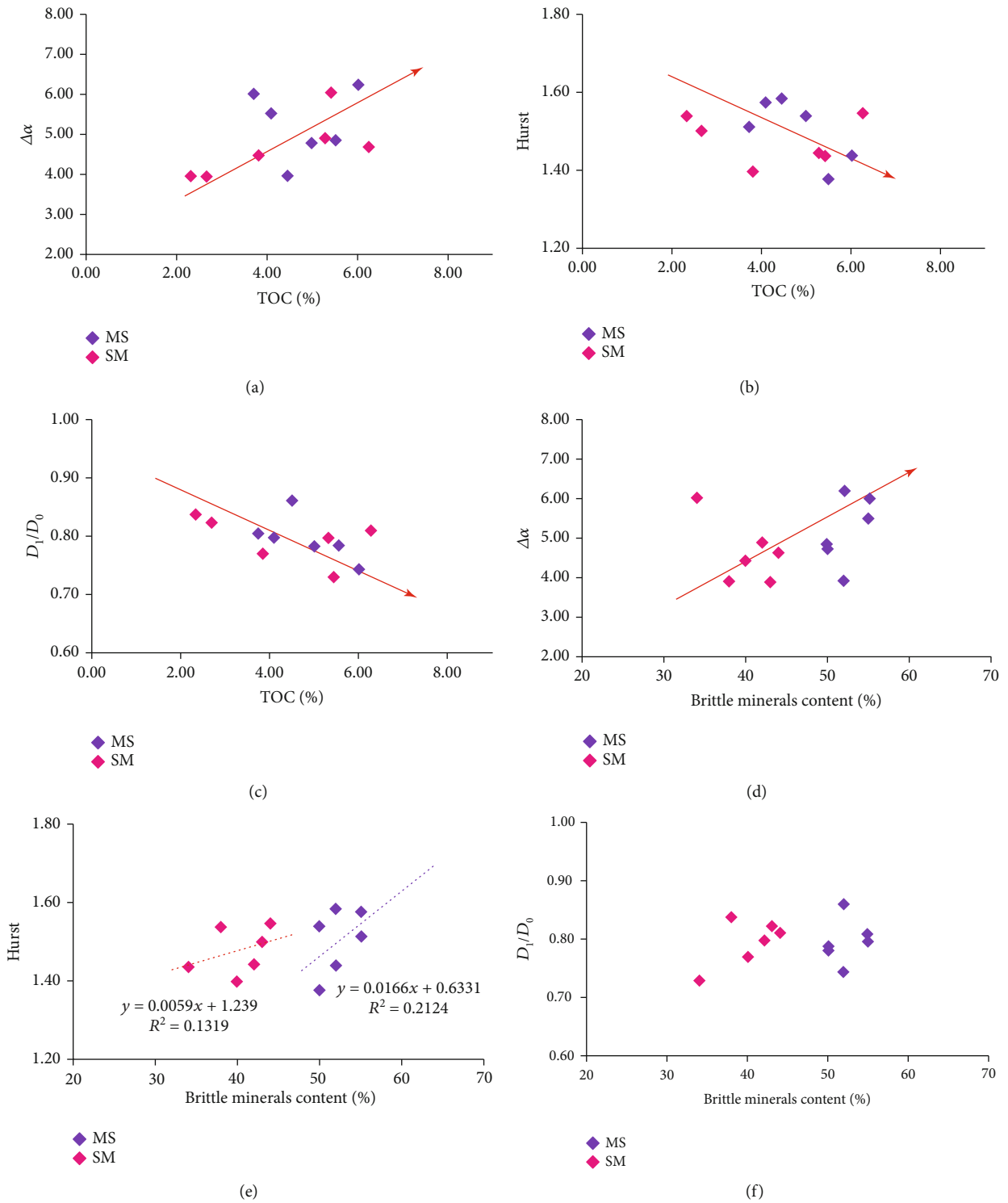
(a)

(b)

(c)

(d)

(e)

(f)
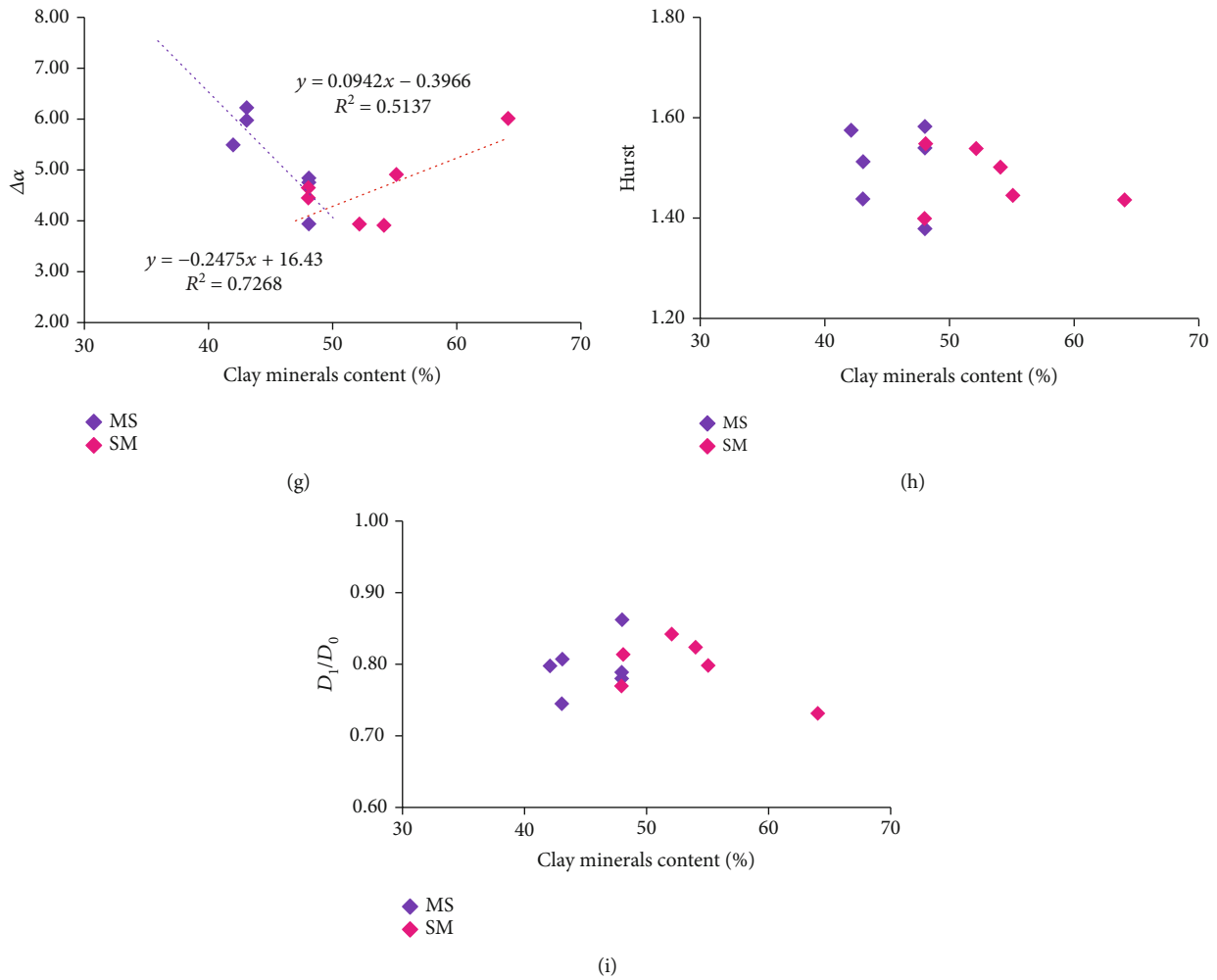
FIGURE 12: Continued.

(g)

(h)

(i)

FIGURE 12: Relationships between total pore volume and TOC (a), total surfer area and TOC (b), total pore volume and clay (c), total surfer area and clay (d), total pore volume and quartz (e), total surfer area and quartz (f), total pore volume and quartz (g), total pore volume and quartz (h), and total pore volume and quartz (h).

to the relationship, the D_1/D_0 is mainly controlled by TPV and TSA. The TPV increases with the various pore size, which results from the larger pore size concentration degree.

5.3. Influence on the Multifractal Characteristics

5.3.1. Effect of TOC. The TOC is the key role of pore volume and surfer area, and the relationships among $\Delta\alpha$, Hurst exponent, D_1/D_0, and the TOC content are established to understand the possible factors affecting the pore structure heterogeneity, pore connection, and the dispersion degree of the MS and SM lithofacies shale (Figures 12(a)–12(c)). The value of $\Delta\alpha$ is of a good positive relationship with the TOC of the MS and SM lithofacies shale samples for wider pore throat size ranging from 2 nm to 200 nm, which suggests the TOC content is the important controlling factor of pore heterogeneous. The pore structure heterogeneous enhances with the increase of TOC content because the TOC itself has more nanoscaled pores and a complex pore network system. This conclusion is consistent with the result of SEM observation and have similar studies in the marine and lacustrine shales [9, 31, 32, 63]. The TOC content has a similar linear relationship with Hurst exponent and D_1/D_0 (Figures 12(b) and 12(c)). The Hurst exponent shows a negative correlation with increasing TOC content (Figure 12(c)) indicating the pore connection decreasing, which is opposite to the result of the previous study [31]. This may be caused by the liquid hydrocarbon block the nanopore structure system in Chang 7 Formation. Similar to the effect of TOC on the pore connection, the D_1/D_0 value of MS and SM lithofacies decreases with the increase in TOC. As for the effect of hydrocarbon generation, some OM pores form with close nanoscale diameters under similar thermal maturity, so that the concentration of PSD would decrease with the TOC increasing [26, 55].

5.3.2. Effect of Rock Compositions. The relationships between different mineral content and the multifractal characteristics parameters ($\Delta\alpha$, Hurst, and D_1/D_0) are plotted to analyze what roles different types of minerals play in the pore structure. As shown in Figure 12(d), the value of $\Delta\alpha$ shows a

positive correlation with brittle mineral content, indicating that the brittle mineral composition is the major factor influencing the value of $\Delta\alpha$. The possible reason for the relationship is that amount of brittle mineral grains can protect the complex OM pore network [13]. There is a generally positive relationship between Hurst exponent and brittle mineral content in both MS and SM lithofacies, which results in the effect of microfractures of shale reservoirs (Figure 12(e)). Compared with the SM lithofacies, the growth of microfracture in the MS lithofacies have a significant potential to form the permeable pore network increasing the pore connectivity. There is no obvious trend of the values for D_1/D_0 with increasing brittle mineral grains, suggesting that quartz has little impact on the concentration degree index (Figure 12(f)).

The cross-plots between the multifractal parameters and clay minerals are established to understand the effect of clay minerals on multifractal parameters (Figures 12(g)–12(i)). The correlations between the $\Delta\alpha$ value and clay content are relatively complicated in different lithofacies, indicating that the characteristic of pores is controlled by various factors (Figure 12(g)). The SM lithofacies values of $\Delta\alpha$ increase slightly with increasing clay content but are negatively correlated with the $\Delta\alpha$ value. This result also suggests the opposite effect of the clay content on the heterogeneity of pore structure in different lithofacies. The clay minerals, with the more complex crystal structure, increase the surface area of pores and improve homogeneous pore structure of the SM lithofacies. Additionally, previous studies about Neijiang formation shale have revealed the same conclusion [7]. However, the low clay contents of the MS lithofacies lead the correlation less obvious. The relationships between the clay and the pore structure heterogeneity parameters are established, which shows no obvious correlation with Hurst (Figure 12(h)). Because the clay content is not the main factor in the pore connection in the Chang 7 Formation. There not exists a linear relationship between D_1/D_0 and clay content, which means the clay minerals have little effect on the dispersion degree (Figure 12(i)).

6. Conclusions

In this study, a series of laboratory experiments (X-ray diffraction, total organic carbon, SEM, and low-pressure N_2 adsorption experiments) and multifractal theory have been conducted to investigate the multifractal dimensions and the pore structure characteristic of lacustrine shales from Chang 7 examples core in south-eastern Ordos Basin, China. The conclusions of this study can be drawn as follows:

(1) Based on the mineral composition characteristics of Chang 7 Formation shales in the Ordos Basin, the Yanchang Formation of Chang 7 shales is divided into two groups: silty mudstone lithofacies and muddy siltstone lithofacies. Compared with the silty mudstone lithofacies, the muddy siltstone lithofacies has a higher siliceous mineral content and TOC content

(2) Different lithofacies have varying total pore volume, total surface area, pore-size distribution, and multifractal dimensions (ranging from 2 nm to 200 nm). The pore volume and surface area of the silty mudstone lithofacies in the studied samples are almost 1.09–1.78 and 0.80–1.72 times greater than those of the muddy siltstone lithofacies samples. In addition to multifractal features, $\Delta\alpha$ values of the muddy siltstone lithofacies are higher than those of the silty mudstone lithofacies, indicating a higher heterogeneity degree of pore size distribution in the muddy siltstone lithofacies

(3) TOC, clay minerals, and siliceous minerals affect the pore structure characteristics and then influence the multifractal parameters. The OM has a positive correlation with the total surface area and pore volume while the relationship between total surface area and the pore volume and mineralogical compositions is complex in both the muddy siltstone and silty mudstone lithofacies. The pore structure of MS lithofacies is mainly affected by the TOC and siliceous mineral contents, and the influence factor for the SM lithofacies is TOC and clay mineral contents. Moreover, there are significant relationships between multifractal parameters ($\Delta\alpha$, H, and D_1/D_0) and pore structure parameters (total pore volume and surfer area) of the silty mudstone and muddy siltstone lithofacies

(4) The TOC of silty mudstone and muddy siltstone lithofacies presents a conspicuous correlation with $\Delta\alpha$, suggesting that the higher the TOC, the more heterogeneous the nanopore structure. Furthermore, the mineralogical compositions have different impacts on $\Delta\alpha$, confirming that the heterogeneity of MS and SM lithofacies could be greatly influenced by the minerals

Data Availability

The data used to support the findings of this study are available from the corresponding authors upon request.

Conflicts of Interest

The authors declare that there are no conflicts of interest regarding the publication of this paper.

Acknowledgments

References

[1] G. R. L. Chalmers and R. M. Bustin, "The organic matter distribution and methane capacity of the Lower Cretaceous strata of Northeastern British Columbia, Canada," *International Journal of Coal Geology*, vol. 70, no. 1-3, pp. 223–239, 2007.

[2] X. Hou, Y. Zhu, S. Chen, Y. Wang, and Y. Liu, "Investigation on pore structure and multifractal of tight sandstone reservoirs in coal-bearing strata using LF-NMR measurements," *Journal of Petroleum Science and Engineering*, vol. 187, p. 106757, 2020.

[3] S. Xu, Q. Gou, F. Hao et al., "Shale pore structure characteristics of the high and low productivity wells, Jiaoshiba shale gas field, Sichuan Basin, China: dominated by lithofacies or preservation condition?," *Marine and Petroleum Geology*, vol. 114, p. 104211, 2020.

[4] D. J. Ross and R. Marc Bustin, "The importance of shale composition and pore structure upon gas storage potential of shale gas reservoirs," *Marine and Petroleum Geology*, vol. 26, no. 6, pp. 916–927, 2009.

[5] P. Zhao, X. Wang, J. Cai et al., "Multifractal analysis of pore structure of Middle Bakken formation using low temperature N_2 adsorption and NMR measurements," *Journal of Petroleum Science and Engineering*, vol. 176, pp. 312–320, 2019.

[6] D. Liu, Z. Li, Z. Jiang et al., "Impact of laminae on pore structures of lacustrine shales in the southern Songliao Basin, NE China," *Journal of Asian Earth Sciences*, vol. 182, p. 103935, 2019.

[7] J. Zhang, Y. Tang, D. He, P. Sun, and X. Zou, "Full-scale nanopore system and fractal characteristics of clay-rich lacustrine shale combining FE-SEM, nano-CT, gas adsorption and mercury intrusion porosimetry," *Applied Clay Science*, vol. 196, p. 105758, 2020.

[8] R. G. Loucks and S. C. Ruppel, "Mississippian Barnett Shale: lithofacies and depositional setting of a deep-water shale-gas succession in the Fort Worth Basin, Texas," *AAPG Bulletin*, vol. 91, no. 4, pp. 579–601, 2007.

[9] R. G. Loucks, R. M. Reed, S. C. Ruppel, and U. Hammes, "Spectrum of pore types and networks in mudrocks and a descriptive classification for matrix-related mudrock pores," *AAPG Bulletin*, vol. 96, no. 6, pp. 1071–1098, 2012.

[10] K. L. Milliken, M. Rudnicki, D. N. Awwiller, and T. Zhang, "Organic matter–hosted pore system, Marcellus formation (Devonian), Pennsylvania," *AAPG Bulletin*, vol. 97, no. 2, pp. 177–200, 2013.

[11] C. R. Clarkson, N. Solano, R. M. Bustin et al., "Pore structure characterization of North American shale gas reservoirs using USANS/SANS, gas adsorption, and mercury intrusion," *Fuel*, vol. 103, pp. 606–616, 2012.

[12] M. E. Curtis, B. J. Cardott, C. H. Sondergeld, and C. S. Rai, "Development of organic porosity in the Woodford Shale with increasing thermal maturity," *International Journal of Coal Geology*, vol. 103, pp. 26–31, 2012.

[13] W. Ji, Y. Song, Z. Jiang et al., "Fractal characteristics of nanopores in the Lower Silurian Longmaxi shales from the Upper Yangtze Platform, South China," *Marine and Petroleum Geology*, vol. 78, pp. 88–98, 2016.

[14] R. Yang, S. He, Q. Hu, M. Sun, D. Hu, and J. Yi, "Applying SANS technique to characterize nano-scale pore structure of Longmaxi shale, Sichuan Basin (China)," *Fuel*, vol. 197, pp. 91–99, 2017.

[15] Z. Song, G. Liu, W. Yang, H. Zou, M. Sun, and X. Wang, "Multi-fractal distribution analysis for pore structure characterization of tight sandstone–a case study of the Upper Paleozoic tight formations in the Longdong District, Ordos Basin," *Marine and Petroleum Geology*, vol. 92, pp. 842–854, 2018.

[16] W. Yang, Y. Song, Z. Jiang et al., "Whole-aperture characteristics and controlling factors of pore structure in the Chang 7th continental shale of the Upper Triassic Yanchang Formation in the southeastern Ordos Basin, China," *Interpretation*, vol. 6, no. 1, pp. T175–T190, 2018.

[17] H. Huang, W. Sun, W. Ji et al., "Effects of pore-throat structure on gas permeability in the tight sandstone reservoirs of the Upper Triassic Yanchang formation in the Western Ordos Basin, China," *Journal of Petroleum Science and Engineering*, vol. 162, pp. 602–616, 2018.

[18] F. Zhang, Z. Jiang, W. Sun et al., "A multiscale comprehensive study on pore structure of tight sandstone reservoir realized by nuclear magnetic resonance, high pressure mercury injection and constant-rate mercury injection penetration test," *Marine and Petroleum Geology*, vol. 109, pp. 208–222, 2019.

[19] X. Zhang, H. Han, J. Peng, and Y. Gou, "Multifractal analysis of pore structure and evaluation of deep-buried Cambrian dolomite reservoir with image processing: a case from Tarim Basin, NW China," *Geofluids*, vol. 2020, Article ID 7131573, 18 pages, 2020.

[20] F. Y. Wang, K. Yang, and Y. Zai, "Multifractal characteristics of shale and tight sandstone pore structures with nitrogen adsorption and nuclear magnetic resonance," *Petroleum Science*, vol. 17, no. 5, pp. 1209–1220, 2020.

[21] X. Li, Z. Jiang, S. Jiang et al., "Characteristics of matrix-related pores associated with various lithofacies of marine shales inside of Guizhong Basin, South China," *Journal of Petroleum Science and Engineering*, vol. 185, p. 106671, 2020.

[22] B. B. Mandelbrot, *The Fractal Geometry of Nature (Vol. 1)*, WH freeman, New York, 1982.

[23] X. Ge, Y. Fan, J. Li, and M. Aleem Zahid, "Pore structure characterization and classification using multifractal theory–an application in Santanghu basin of western China," *Journal of Petroleum Science and Engineering*, vol. 127, pp. 297–304, 2015.

[24] K. Liu, M. Ostadhassan, J. Zou et al., "Multifractal analysis of gas adsorption isotherms for pore structure characterization of the Bakken Shale," *Fuel*, vol. 219, pp. 296–311, 2018.

[25] K. Liu, M. Ostadhassan, J. Zou et al., "Nanopore structures of isolated kerogen and bulk shale in Bakken Formation," *Fuel*, vol. 226, pp. 441–453, 2018.

[26] S. Zheng, Y. Yao, D. Liu, Y. Cai, Y. Liu, and X. Li, "Nuclear magnetic resonance T_2 cutoffs of coals: a novel method by multifractal analysis theory," *Fuel*, vol. 241, pp. 715–724, 2019.

[27] A. Dathe, S. Eins, J. Niemeyer, and G. Gerold, "The surface fractal dimension of the soil-pore interface as measured by image analysis," *Geoderma*, vol. 103, no. 1-2, pp. 203–229, 2001.

[28] P. Zhao, Z. Wang, Z. Sun, J. Cai, and L. Wang, "Investigation on the pore structure and multifractal characteristics of tight oil reservoirs using NMR measurements: Permian Lucaogou Formation in Jimusaer Sag, Junggar Basin," *Marine and Petroleum Geology*, vol. 86, pp. 1067–1081, 2017.

[29] A. Li, W. Ding, K. Jiu, Z. Wang, R. Wang, and J. He, "Investigation of the pore structures and fractal characteristics of marine shale reservoirs using NMR experiments and image analyses: a case study of the Lower Cambrian Niutitang Formation in northern Guizhou Province, South China," *Marine and Petroleum Geology*, vol. 89, pp. 530–540, 2018.

[30] L. Tang, Y. Song, Z. Jiang, S. Jiang, and Q. Li, "Pore structure and fractal characteristics of distinct thermally mature shales," *Energy & Fuels*, vol. 33, no. 6, pp. 5116–5128, 2019.

[31] Y. Li, Z. Wang, Z. Pan, X. Niu, Y. Yu, and S. Meng, "Pore structure and its fractal dimensions of transitional shale: a cross-section from east margin of the Ordos Basin, China," *Fuel*, vol. 241, pp. 417–431, 2019.

[32] C. Shan, W. F. Zhao, K. Wang et al., "Nanoscale pore structure heterogeneity and its quantitative characterization in Chang7 lacustrine shale of the southeastern Ordos Basin, China," *Journal of Petroleum Science and Engineering*, vol. 187, p. 106754, 2020.

[33] X. Wang, Y. Zhu, and Y. Wang, "Fractal characteristics of Micro- and mesopores in the Longmaxi Shale," *Energies*, vol. 13, no. 6, p. 1349, 2020.

[34] D. Liu, T. Tian, R. Liang, F. Yang, and F. Ye, "Characterization of shale pore structure by multitechnique combination and multifractal analysis and its significance," *Geofluids*, vol. 2020, Article ID 8896940, 16 pages, 2020.

[35] R. Lopes and N. Betrouni, "Fractal and multifractal analysis: a review," *Medical Image Analysis*, vol. 13, no. 4, pp. 634–649, 2009.

[36] W. Li, H. Liu, and X. Song, "Multifractal analysis of Hg pore size distributions of tectonically deformed coals," *International Journal of Coal Geology*, vol. 144-145, pp. 138–152, 2015.

[37] L. Zhang, G. Bai, X. Luo et al., "Diagenetic history of tight sandstones and gas entrapment in the Yulin Gas Field in the central area of the Ordos Basin, China," *Marine and Petroleum Geology*, vol. 26, no. 6, pp. 974–989, 2009.

[38] Y. Yang, C. Liang, J. Zhang, Z. Jiang, and X. Tang, "A developmental model of lacustrine shale gas genesis: a case from T_3y^7 shale in the Ordos Basin, China," *Journal of Natural Gas Science and Engineering*, vol. 22, pp. 395–405, 2015.

[39] J. WANG and J. WANG, "Low-amplitude structures and oil-gas enrichment on the Yishaan Slope, Ordos Basin," *Petroleum Exploration and Development*, vol. 40, no. 1, pp. 52–60, 2013.

[40] J. Dai, J. Li, X. Luo et al., "Stable carbon isotope compositions and source rock geochemistry of the giant gas accumulations in the Ordos Basin, China," *Organic Geochemistry*, vol. 36, no. 12, pp. 1617–1635, 2005.

[41] R. Y. Chen, X. R. Luo, Z. K. Chen, J. Yu, and B. Yang, "Restoration of burial history of four periods in Ordos Basin," *Acta Petrolei Sinica*, vol. 27, pp. 43–47, 2006.

[42] H. Yang and W. Z. Zhang, "Leading effect of seventh member high-quality source rock of Yanchang formation in Ordos Basin during the enrichment of low-penetrating oilgas accumulation: geology and geochemistry," *Geochimica*, vol. 34, pp. 147–154, 2005.

[43] W. Zhang, W. Yang, and L. Xie, "Controls on organic matter accumulation in the Triassic Chang 7 lacustrine shale of the Ordos Basin, Central China," *International Journal of Coal Geology*, vol. 183, pp. 38–51, 2017.

[44] Y. Cao, H. Han, C. Guo, P. Pang, Z. G. Ding, and Y. Gao, "Influence of extractable organic matters on pore structure and its evolution of Chang 7 member shales in the Ordos Basin, China: implications from extractions using various solvents," *Journal of Natural Gas Science and Engineering*, vol. 79, p. 103370, 2020.

[45] J. Rouquerol, P. Llewellyn, and F. Rouquerol, "Is the bet equation applicable to microporous adsorbents?," *Studies in Surface Science and Catalysis*, vol. 160, no. 7, pp. 49–56, 2007.

[46] M. Guan, X. Liu, Z. Jin, and J. Lai, "The heterogeneity of pore structure in lacustrine shales: Insights from multifractal analysis using N_2 adsorption and mercury intrusion," *Marine and Petroleum Geology*, vol. 114, p. 104150, 2020.

[47] M. Liu, R. Xie, J. Guo, and G. Jin, "Characterization of pore structures of tight sandstone reservoirs by multifractal analysis of the NMR T_2 distribution," *Energy & Fuels*, vol. 32, no. 12, pp. 12218–12230, 2018.

[48] J. P. Ferreiro, M. Wilson, and E. V. Vázquez, "Multifractal description of nitrogen adsorption isotherms," *Vadose Zone Journal*, vol. 8, no. 1, pp. 209–219, 2009.

[49] T. C. Halsey, M. H. Jensen, L. P. Kadanoff, I. Procaccia, and B. I. Shraiman, "Fractal measures and their singularities: the characterization of strange sets," *Physical Review A*, vol. 33, no. 2, pp. 1141–1151, 1986.

[50] J. F. Gouyet, M. Rosso, and B. Sapoval, "Fractal surfaces and interfaces," in *Fractals and Disordered Systems*, pp. 263–302, Springer, Berlin, Heidelberg, 1996.

[51] P. Grassberger, "Generalized dimensions of strange attractors," *Physics Letters A*, vol. 97, no. 6, pp. 227–230, 1983.

[52] P. Wang, Z. Jiang, L. Yin et al., "Lithofacies classification and its effect on pore structure of the Cambrian marine shale in the Upper Yangtze Platform, South China: evidence from FE-SEM and gas adsorption analysis," *Journal of Petroleum Science and Engineering*, vol. 156, pp. 307–321, 2017.

[53] H. Yu, Z. Wang, F. Wen et al., "Reservoir and lithofacies shale classification based on NMR logging," *Petroleum Research*, vol. 5, no. 3, pp. 202–209, 2020.

[54] M. He, H. Gu, and H. Wan, "Log interpretation for lithology and fluid identification using deep neural network combined with MAHAKIL in a tight sandstone reservoir," *Journal of Petroleum Science and Engineering*, vol. 194, p. 107498, 2020.

[55] C. Dong, C. Ma, C. Lin, X. Sun, and M. Yuan, "A method of classification of shale set," *Journal of China University of Petroleum*, vol. 39, no. 3, pp. 1–7, 2015.

[56] C. Xue, J. Wu, L. Qiu et al., "Lithofacies classification and its controls on the pore structure distribution in Permian transitional shale in the northeastern Ordos Basin, China," *Journal of Petroleum Science and Engineering*, vol. 195, p. 107657, 2020.

[57] Z. Ren, S. Zhang, S. L. Gao, J. P. Cui, Y. Y. Xiao, and H. Xiao, "Tectonic thermal history and its significance on the formation of oil and gas accumulation and mineral deposit in Ordos Basin," *Science in China Series D: Earth Sciences*, vol. 50, no. S2, pp. 27–38, 2007.

[58] S. J. Gregg, K. S. Sing, and K. S. Sing, *Adsorption, Surface Area and Porosity*, vol. 86, Academic Press, London, 1982.

[59] J. Landers, G. Y. Gor, and A. V. Neimark, "Density functional theory methods for characterization of porous materials," *Colloids and Surfaces A: Physicochemical and Engineering Aspects*, vol. 437, pp. 3–32, 2013.

[60] O. K. Ozotta, K. Liu, T. Gentzis et al., "Pore structure alteration of organic-rich shale with Sc-CO_2 exposure: the Bakken Formation," *Energy & Fuels*, vol. 35, no. 6, pp. 5074–5089, 2021.

[61] K. S. W. Sing, "Reporting physisorption data for gas/solid systems with special reference to the determination of surface area and porosity (recommendations 1984)," *Pure and Applied Chemistry*, vol. 57, no. 4, pp. 603–619, 1985.

[62] X. Chen, X. Qu, S. Xu et al., "Dissolution pores in shale and their influence on reservoir quality in Damintun Depression, Bohai Bay Basin, East China: insights from SEM images, N_2

adsorption and fluid-rock interaction experiments," *Marine and Petroleum Geology*, vol. 117, p. 104394, 2021.

[63] E. V. Vázquez, J. P. Ferreiro, J. G. V. Miranda, and A. P. González, "Multifractal analysis of pore size distributions as affected by simulated rainfall," *Vadose Zone Journal*, vol. 7, no. 2, pp. 500–511, 2008.

[64] X. Ge, Y. Fan, X. Zhu, Y. Chen, and R. Li, "Determination of nuclear magnetic resonance T_2 cutoff value based on multifractal theory—an application in sandstone with complex pore structure," *Geophysics*, vol. 80, no. 1, pp. D11–D21, 2015.

[65] R. Holmes, E. C. Rupp, V. Vishal, and J. Wilcox, "Selection of shale preparation protocol and outgas procedures for applications in low-pressure analysis," *Energy & Fuels*, vol. 31, no. 9, pp. 9043–9051, 2017.

[66] C. Zhou, N. Liang, and Z. Liu, "Multifractal characteristics of pore structure of red beds soft rock at different saturations," *Journal of Engineering Geology*, vol. 28, no. 1, pp. 1–9, 2020.

[67] A. Li, W. Ding, J. He, P. Dai, S. Yin, and F. Xie, "Investigation of pore structure and fractal characteristics of organic-rich shale reservoirs: a case study of Lower Cambrian Qiongzhusi formation in Malong block of eastern Yunnan Province, South China," *Marine and Petroleum Geology*, vol. 70, pp. 46–57, 2016.

[68] T. Li, Z. Jiang, Z. Li et al., "Continental shale pore structure characteristics and their controlling factors: a case study from the lower third member of the Shahejie Formation, Zhanhua Sag, Eastern China," *Journal of Natural Gas Science and Engineering*, vol. 45, pp. 670–692, 2017.

[69] H. Fu, X. Wang, L. Zhang et al., "Investigation of the factors that control the development of pore structure in lacustrine shale: a case study of block X in the Ordos Basin, China," *Journal of Natural Gas Science and Engineering*, vol. 26, pp. 1422–1432, 2015.